



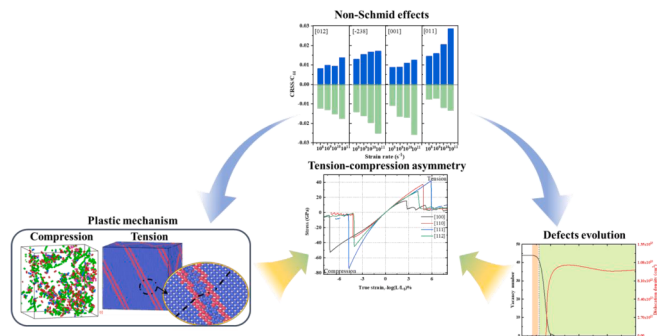
## Heterogeneous nucleation of plastic defects and tension-compression asymmetry in the presence of vacancies in W single crystals

Ziyi Li, Wensheng Liu, Yunzhu Ma, Chaoping Liang<sup>\*</sup>

National Key Laboratory of Science and Technology for High-strength Structural Materials, Central South University, Changsha 410083, China



### GRAPHICAL ABSTRACT



### ARTICLE INFO

#### Keywords:

Molecular dynamics  
Tension-compression asymmetry  
Plastic deformation  
Screw dislocation  
Vacancy

### ABSTRACT

The tension-compression asymmetry with pre-existing vacancies is investigated for tungsten using molecular dynamics (MD). The tension-compression asymmetry is revealed by means of uniaxial tension and compression along [100], [110], [111], and [112] crystallographic orientations with different strain rates ( $10^8 \sim 10^{11} \text{ s}^{-1}$ ). Results show that except for [110] loading orientation, the yield stresses in compressive are generally greater than those in tensile loading. Vacancy narrows the tension-compression asymmetry as it reduces the gap between tensile and compressive yield strengths when the vacancy concentration goes up. This is through the coalescence of individual vacancy into vacancy clusters before yielding. Aggregation and coalescence of vacancies before yielding lead to the formation of different types of defects, facilitating plastic deformations at yielding. Thus, various plastic deformation mechanisms, like vacancy dislocation loops, twinning, anti-twinning, etc., are observed in tension and compression along different crystallographic orientations. Owing to the non-planar cores,  $1/2\langle 111 \rangle$  screw dislocation is identified as the manipulator behind those plastic deformations. The critical resolved shear stress (CRSSs) on the maximum resolved shear stress plane (MRSSP) for the  $1/2\langle 111 \rangle$  screw dislocation loaded in tension and compression are determined and responsible for the origin of tension-compression asymmetry in tungsten.

\* Corresponding author.

E-mail address: [cpliang@csu.edu.cn](mailto:cpliang@csu.edu.cn) (C. Liang).

## 1. Introduction

Tungsten (W) due to its high melting point, high resistance to sputtering and low tritium retention is considered as the primary choice of plasma-facing material (first wall) in fusion reactor [1,2]. Vacancies, as one of the most typical defects, are easily generated when tungsten is exposed in high dose of neutron irradiation (14 MeV-peaked neutron spectrum). Besides the neutron irradiation, high thermal flux ( $\sim 10$  MW/m $^2$ ) induces cyclic stress on the first wall, exerting potential mechanical failure during the long-term service of fusion reactor. It is thus of great importance to investigate how vacancies influence the mechanical response and corresponding material behaviors of tungsten, in particular, the cyclic tension-compression asymmetry under high strain rate loading.

Tension-compression asymmetry is well expected for body-centered cubic (BCC) tungsten [3–5]. According to Neumann's principle [6], the slip direction of BCC metals is the closest packed {111} directions. The corresponding {111} are not the close-packed plane and has no mirror plane. As a result, the flow stress will not be the same when the sign of the loading direction and resolved shear stress in the slip system is reversed. For example, Kim et al. [7] found that bcc nanopillars exhibit pronounced tension-compression asymmetry, with strain-hardening under tension significantly lower than in compression, resulting in flow stresses under tension only 60 % of those in compression. Similarly, Irwin et al. [8] observed this asymmetry in single-crystal Mo, where the yielding stress for compression along the [111] orientation was approximately 600 MPa, compared to about 400 MPa for tension. Up to now, advanced experimental characterization and molecular dynamics (MD) have been utilized to reveal the intrinsic mechanism behind tension-compression asymmetry in BCC metals [3,4,7,9,10]. It was found that the loading direction plays a key role in tension-compression asymmetry with the help of various plastic behaviors. For instance, Wang et al. [5] discovered that twinning and anti-twinning induces the tension-compression asymmetry in [110]-oriented W nanowires. Ta, next to W on periodic table, also shows tension-compression asymmetry. Wang and Beyerlein [11] investigated tension-compression asymmetry of single crystal Ta in the [100], [110] and [111] directions. The non-Schmid effects for {110} and {112} slip result in anisotropy and asymmetry in the stress-strain response of single crystal Ta. Bertin et al. [12] studied the mechanical response of single crystal BCC metal through MD simulations and attributed tension-compression asymmetry behavior to the twinning/anti-twinning asymmetry of shears on the {112} planes. On the other hand, Healy and Ackland [9] unraveled different plastic deformation mechanisms in BCC Fe under [100] compression and tension. In compression the plastic deformation is mediated by dislocations, while it occurs through the creation and motion of twin boundaries in tension. In addition, non-Schmidt stress out of the slip plane and the corresponding screw dislocation nucleation and motion were related to the tension-compression asymmetry. However, the above-mentioned plastic behaviors were affiliated to particular crystal direction, there lacks a systematical understanding among different crystallographic orientations.

Irradiation damage generally results in the formation of both interstitials and vacancies, with both defect types tending to cluster and subsequently act as nucleation sites for dislocations or twins during plastic deformation [13,14]. However, in molecular dynamics simulations, interstitial W often returns to their original lattice positions as the system seeks to minimize huge defect energy, whereas vacancies, which remain stable and randomly distributed after relaxation. Besides, there are different types of sinks, highly biased towards interstitials, resulting in a strong bias for vacancy production [15–17], provides a more suitable model for investigating tension-compression asymmetry in irradiated tungsten [18]. Current studies on vacancies in W focused on the generation and evolution during collision cascades [19–23]. MD was widely adopted to describe the recombination and consequent line

(dislocation rings), plane (grain boundaries), or bulk (voids) defects in the single crystal W [24–28]. It is well known that vacancies can significantly influence the plastic deformation behaviors, like dislocation glide and twinning [29–31]. For example, Dutta [32] found that vacancies arrest motion of screw dislocation in Fe towards to vacancies, triggering its immediate dissociation into a twin nucleus. However, the vacancy assisted plastic behaviors in tension-compression asymmetry were seldomly reported, and those in W would be more pronounced as a result of its high strength and poor ductility.

In order to understand the tension-compression asymmetry in the presence of vacancies in W, we have applied uniaxial compression and tension on low-index [100], [110], [111] and [112] crystal direction by means of MD simulations. The detailed plastic behaviors, like dislocation nucleation and propagation, twinning and anti-twinning, etc., were revealed and their relationship with tension-compression asymmetry was determined. The simulated results were compared with available experimental observation. Moreover, the intrinsic mechanism was unraveled with quantitative analyses. The rest of this paper was organized as follows. Section 2 gives the settings of molecular dynamics simulation, as well as the characteristic methods for tracking the defects, such as dislocations and twins. In Section 3, the stress-strain response was recorded. The results of the tension-compression asymmetry and associated plastic behaviors were discussed in detail in this section. Further interpretations about the results are shown in Section 4. Concluding remarks were summarized in Section 5.

## 2. Computational model and method

We employed the open-source molecular dynamics (MD) code LAMMPS [33] to investigate the plastic behavior of BCC tungsten with various vacancy volume fractions subjected to strain rates ranging from  $10^8$  s $^{-1}$  to  $10^{11}$  s $^{-1}$ . The interatomic potential used in our simulations was based on a semiempirical model developed by Zhou et al. [34], which utilizes the embedded atom method (EAM) to describe the interactions between tungsten atoms. This potential not only reproduces correct point defect structure and dislocation behavior but also has been extensively validated in the literature [35–39]. We conducted independent tests on lattice constants, elastic constants, phonon dispersion curves, equation of states. More importantly, the stacking faults, static energies, migration barriers and core structures are also tested to prove that the EAM potential can predict the point defect and dislocation behavior well. The test results are shown in Fig. S1, Fig. S2, Table S1 and S2 of supplementary material. The good agreement between our MD results and the first-principles calculations and experiments demonstrates the reliability and accuracy of Zhou et al.'s potential [34]. Besides, Zhou et al.'s potential [34] has been successfully used to simulate the plastic behaviors of tungsten with nanovoid [40], indicating it is suitable for modeling defects evolution. Four initial single crystal structures consist of 221,184, 442,368, 884,736 and 884,736 atoms were created for loading orientations [100], [110], [111] and [112] crystal direction, respectively. Larger cell size was also tested and compared with the setting adopted in this paper, including the mechanical response (stress-strain curves) and plastic deformation mechanisms, which are almost the same across different cell sizes (as shown in Fig. S3 and S4). Specifically, for [100], the orthotropic crystal orientations [100], [010] and [001] were aligned along the x-, y- and z-axes, respectively. Correspondingly, they were [110], [110] and [001] for [110], [111], [110] and [112] for [111], and [112], [111] and [110] for [112], respectively. Periodic boundary conditions were applied in all three Cartesian directions. To model the vacancy distribution, atoms were then randomly removed from the perfect crystal structures to achieve an initial vacancy concentration 0.02 %, 0.532 % and 1.029 %. The constructed defective structures were further equilibrated by the conjugate gradient (CG) minimization method.

After the model was constructed, the defective system was firstly

subjected to thermalization under the isothermal-isobaric ensemble (NPT) at a temperature of 300 K and zero pressure. The relaxation process lasted for 200 ps with a time step of 10 fs. Secondly, uniaxial compressive strain and tensile strain were applied to the simulation box at the prescribed strain rate, while maintaining a constant temperature of 300 K using NPT ensemble. Seven strain rates  $10^8$ ,  $5 \times 10^8$ ,  $10^9$ ,  $5 \times 10^9$ ,  $10^{10}$ ,  $5 \times 10^{10}$ , and  $10^{11} \text{ s}^{-1}$  were considered in this work. The strain rate is applied through changing a dimension of the box at a “constant engineering strain rate”. The strain is obtained by calculating the variation of the length along loading axis Lx. The simulations were continued until the ‘longest’ dimension (Lx) of the system was compressed to one-fourth of its initial size. The total duration of the simulations is 3000 ps. To accurately capture the atomistic behavior during yielding, we employed very small timesteps in the simulations depending on strain rates, ranging from 1 fs ( $10^9 \text{ s}^{-1}$ ,  $10^{10} \text{ s}^{-1}$  and  $10^{11} \text{ s}^{-1}$ ) to 10 fs ( $10^8 \text{ s}^{-1}$ ). Although 10 fs is relatively large for MD simulations, we have compared the total energy using timestep of 1 fs and 10 fs as shown in Fig. S5 and the results indicate conversion of total energy at this larger timestep in the driven system. While the strain rates employed in our simulations exceed those typical of most tensile or compressive experiments, the observed dislocation activities, defect interactions, and phase transformations are consistent across both high and low strain rates based on our tests. The strain rates in this work, like  $10^8 \text{ s}^{-1}$ , were employed by Wang et al. [5] and to confirm their TEM observation on W nanowire under  $\langle 110 \rangle$  tension. The consistency between experimental observation and MD simulation is quite well. Finally, the formed defects are analyzed using Open Visualization Tool (OVITO) [41] through the common neighbor analysis (CNA) [42] and dislocation extraction algorithm (DXA) [43].

We also simulated motion of bcc  $1/2\langle 111 \rangle$  screw dislocation core under tension-compression asymmetry, which was based on the work in the literature [3,44,45]. The details are as follows. We used a block consisted of 14400 atoms that the z-axis coincides with the Burgers vector and the direction of the dislocation line ([111] orientation), the y-axis is along  $\langle \bar{1}01 \rangle$ . The x-axis is orthogonal to both y-axis and z-axis, and the initial size is  $76 \text{ \AA} \times 54 \text{ \AA} \times 6 \text{ \AA}$ . A  $1/2\langle 111 \rangle$  screw dislocation was considered in the block according to the anisotropic elastic strain filed [46]. The periodic boundary is applied to z-direction ([111]) to simulate an infinitely long straight screw dislocation. The block of atoms was divided into an active part and inactive part (see Fig. 1), in which the atoms in active part were relaxed, while holding the atoms in the inactive part fixed. The relaxation of core structure was conducted until the forces act on all atoms fell below  $0.01 \text{ \AA}^{-1}$ .

In order to evaluate the critical resolved shear stress (CRSS), an external stress was applied. The elastic displacement field corresponding to this stress was evaluated using anisotropic elasticity and superimposed on the dislocation displacement field for the atoms in both the active and inactive parts. The atoms in the active region were subsequently relaxed by minimizing the total energy of the block, similar to the non-stressed case. The aim of these calculations was to determine the

stress at which the dislocation begins to move and to identify the actual glide plane. Since vacancies have the lowest dislocation-vacancy interaction energy when they stay on the dislocation core [47], we remove an atom from the dislocation core to create a vacancy and relax the core structure again. To simulate the tension-compression asymmetry, the constant velocity method is applied [48,49] and the stress tensor applied in this study has the form of

$$\Sigma_{\tau,\sigma} = \begin{bmatrix} -\tau & 0 & 0 \\ 0 & \tau & \sigma \\ 0 & \sigma & 0 \end{bmatrix}.$$

### 3. Results

#### 3.1. flow stress of tension and compression

The flow stresses of BCC tungsten with vacancies from 0.02 % to 1.029 % at constant strain rate ( $\dot{\epsilon}$ ) of  $10^8$ ,  $5 \times 10^8$ ,  $10^9$ ,  $5 \times 10^9$ ,  $10^{10}$ ,  $5 \times 10^{10}$ , and  $10^{11} \text{ s}^{-1}$  were determined by MD. Fig. 2 shows the typical examples of flow stress for tungsten to be loaded by compression and tension along crystallographic orientations [100], [110], [111], and [112] at  $\dot{\epsilon} = 10^8 \text{ s}^{-1}$ . Several features could be seen from this figure.

Firstly, obvious tension-compression asymmetry can be observed in the strain-stress curves. The yield stresses under uniaxial compression loadings are generally larger than those in uniaxial tension loadings. For instance, the yield stresses for compression along [100], [111], and [112] are 52.9, 74.3, 45.1 GPa, respectively, while those for uniaxial tension are only 15.2, 43.0, 27.9 GPa (Fig. 2(a)), respectively. The yield stresses under uniaxial tension are almost half of those under compression condition. In the literature, Fe, Mo, and Ta [4,7,9,50] also have the uniaxial compression loading with a higher yield stress than uniaxial tension loading. It should be noted the yield stresses predicted from MD are generally an order of magnitude higher than the experimental counterpart [9,51]. This originates from the factor that the situation in MD simulation is near “ideal”, while in real world experimental samples are teemed with defects. However, the plastic mechanisms related to the tension or compression are comparable, as demonstrated in the literature [4,5,7]. On the other hand, in uniaxial loading along the [110] orientation, an intriguing phenomenon is observed. It exhibits a yield point at a stress of 37.3 GPa under tension, surpassing the corresponding compression threshold of 32.4 GPa. In previous investigations about tension-compression asymmetry, Farkas et al. [52,53] believed that the yield stress may not be the most accurate representation of the material’s yield behavior due to the potential overshooting effects associated with high strain rates and dislocation-free microstructures in MD simulations. Thus, the flow stresses after yielding for different orientations under uniaxial compression and tension are calculated as shown in Fig. S6. The same tension-compression asymmetry trend persists.

Secondly, the magnitude of tension-compression asymmetry is deduced from the gap of yield strength, which exhibits strong crystal orientation dependence in uniaxial loading along [100], [110], [111], and [112]. As shown in Fig. 2(a), even though the yield strengths for both of tension and compression along [111] are the largest, there is a huge difference in yield strength between them, which leads to the highest tension-compression asymmetry. For other three orientations, [110] shows the smallest yield strength under uniaxial tension, while the largest along [112] among them. However, the yield strengths of [100], [110] and [112] change completely in the opposite direction under uniaxial compression. Closer examination indicates that the gap in yield strength between tension and compression along [100], [110] and [112] orientations are 56.3, 62.9 and 65.81 GPa, respectively. Thus, the magnitude of tension-compression asymmetry follows the sequence of [111] > [112] > [110] > [100]. As shown in Fig. 2, the vacancy concentrations seem do not change this trend.

Thirdly, the influence of vacancy concentrations becomes significant in tension-compression asymmetry, exhibiting a decreasing trend with increased vacancy concentration in all four loading orientations. The

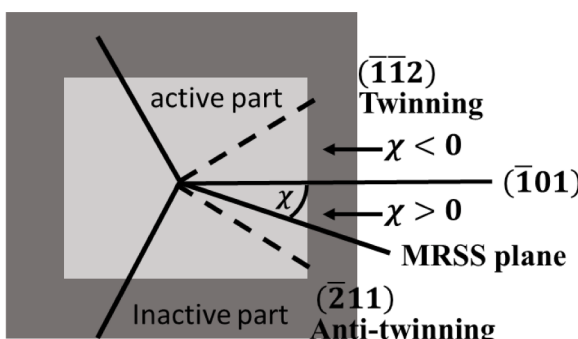
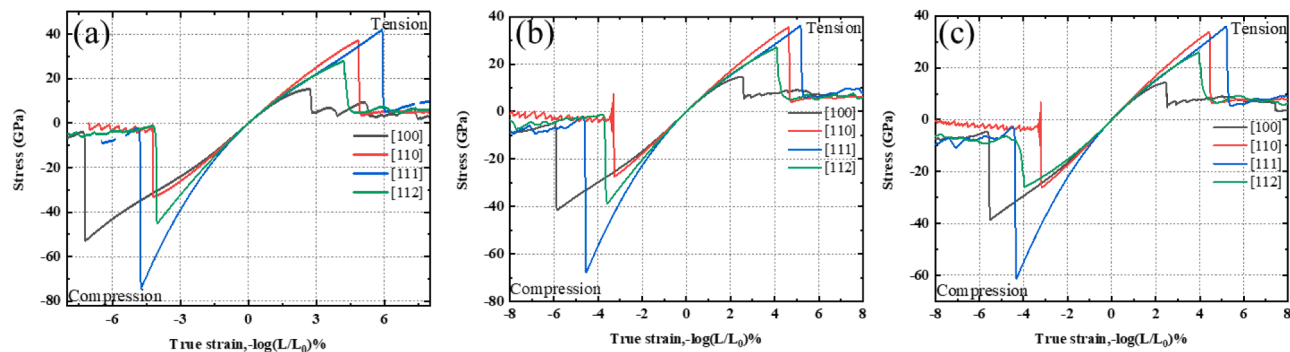


Fig. 1. Schematic picture of the block used in the calculations.



**Fig. 2.** Stress-strain curves for single crystal tungsten with different vacancy concentrations in tension and compression at strain rate of  $10^8 \text{ s}^{-1}$ . (a) Vacancy concentration 0.020 %. (b) Vacancy concentration 0.532 %. (c) Vacancy concentration 1.029 %.

influence of vacancies is more pronounced in compression compared to tension. For instance, in the case of uniaxial compression along the [111] direction, the yield stress decreased from 74.3 GPa with the vacancy concentration of 0.02 % to 61.4 GPa with the vacancy concentration of 1.029 %, resulting in 17.4 % stress reduction. For uniaxial tension, the yield stress decreased from 14.7 GPa with the vacancy concentration of 0.02 % to 14.3 GPa with the vacancy concentration of 1.029 %, only resulting in 2.7 % stress reduction. Thus, the gap in yield strength between tension and compression becomes smaller with the increase of vacancy concentration.

### 3.2. Defect evolution under tension-compression asymmetry

The plastic response of tungsten containing vacancies exhibits notable characteristics across various crystallographic orientations. In

order to gain deeper insights into the tension-compression asymmetry of single crystal tungsten and the ones with vacancies, we conducted a comparative analysis of the microstructural evolution under different loading conditions. Vacancies in our simulation samples are distributed randomly, the atomic structures remained stable in time and show the same deformation mechanisms with three different vacancy concentrations (0.020 %, 0.532 % and 1.029 %). Therefore, we mainly take vacancy concentration 0.02 % as a typical example. For interested readers, the case of vacancy concentration 1.029 % is analyzed in Fig. S7 of supplementary material for comparison. The specific plastic behaviors are described in detail based on the loading directions.

#### (1) Loading along [100]

As illustrated in Fig. 3(a), tensile loading initiates the interaction of

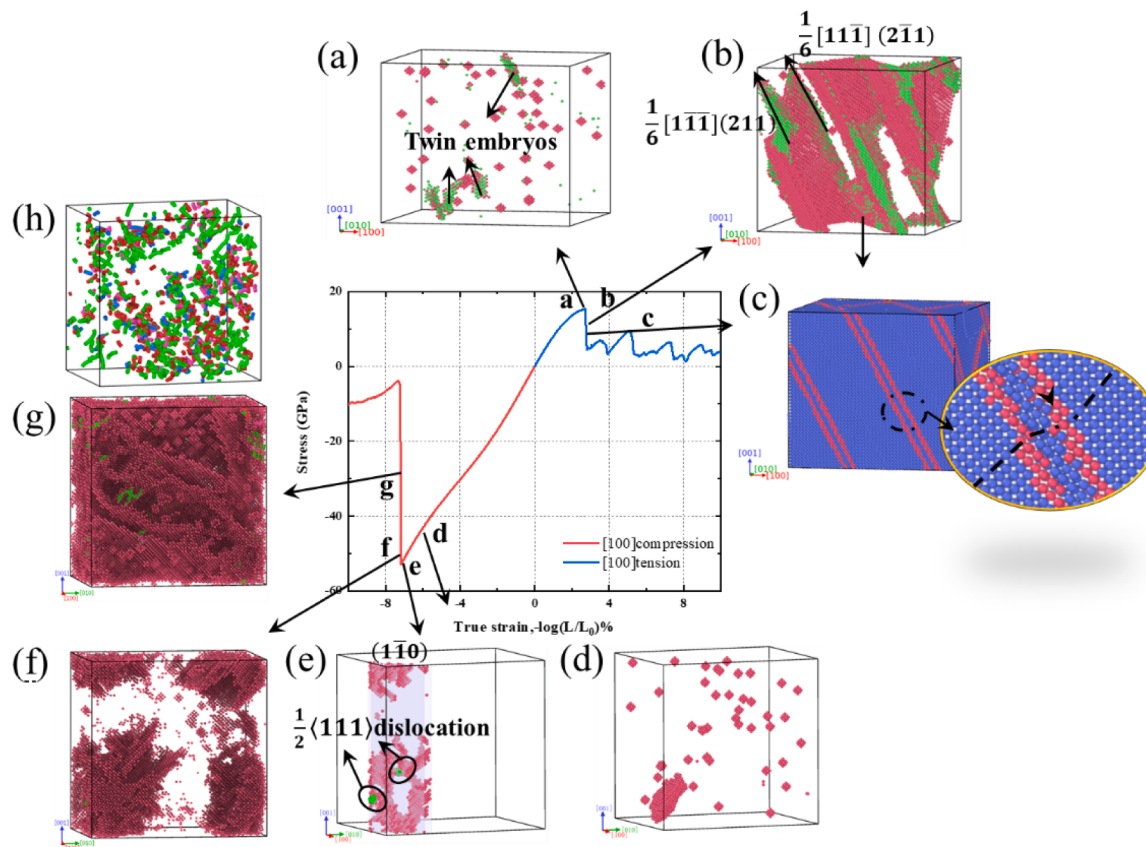


**Fig. 3.** Snapshots of atomistic configuration during tension deformation process ((a)  $\varepsilon = 2.69\%$ , (b)  $\varepsilon = 2.74\%$ , (c)  $\varepsilon = 2.77\%$ ) and compression deformation process ((d)  $\varepsilon = -6.21\%$ , (e)  $\varepsilon = -7.05\%$ , (f)  $\varepsilon = -7.25\%$ , (g)  $\varepsilon = -7.31\%$ ) at strain rate  $10^8 \text{ s}^{-1}$  along [100] orientation (vacancy concentration 0.02 %).

isolated vacancies, leading to the nucleation of twin embryos, which marks the onset of yielding. As the tensile loading continued, these twin embryos merged with the help of neighboring vacancies, resulting in the formation of  $(211)$  and  $(2\bar{1}\bar{1})$  stacking faults (see Fig. 3(b)). These faults subsequently transform into two symmetric twins. By using the CNA analysis, the zoom-in picture of these twin boundaries is clearly shown in Fig. 3(c).

Similarly, Fig. 3(d) - (h) show the defect evolution of single tungsten under compressive loading. In Fig. 3(d), during the elastic deformation stage, the individual vacancies interact with each other to form defect clusters which act as the potential nucleation sites for partial dislocations. The process of vacancy reaction is shown in Fig. S8 of supplementary material that the interaction between vacancy labelled #2 and #3 gradually leads to the formation of a rod-shaped vacancy cluster under continuous compressive loading. With time going on, in the growth process of this vacancy cluster structure, it will merge the surrounding vacancies like vacancy #1 to form a strip-shaped vacancy cluster structure. The nucleation of  $1/2(111)$  partial dislocations occur at  $\epsilon = 7.05\%$  as shown in Fig. 3(e). With the increase of strain, as shown in Fig. 3(f), stacking faults bounded by partial dislocations are the primary form of plastic mechanism after yielding. These stacking faults originate from the emission and propagation of Shockley partial dislocations and expand along the equivalent  $(112)$  plane and eventually fill the entire unit cell (Fig. 3(g)). The defect structure is captured in Fig. S9 of supplementary material. Fig. 3(h) displays the visualization of final dislocation morphology. Note that, a part of perfect dislocations reacted with each other to generate  $(100)$ -type dislocations (colored with purple) and  $(110)$ -type dislocations (colored with blue) through

$$\frac{1}{2}(111) + \frac{1}{2}(\bar{1}\bar{1}\bar{1}) \rightarrow (100) \quad (1)$$



Lots of short dislocation segments accompanied with stacking faults contribute to a rapid decrease in flow stress under compressive loading condition.

## (2) Loading along [110]

For tensile and compressive loadings along [110] orientation, there is a dynamic competition between dislocation slip and deformation twinning during the plastic deformation in tungsten with vacancies. Fig. 4(a) shows the nucleation of stacking faults from vacancies during elastic deformation stage. Subsequently, as the stress increases, dislocation nucleation occurs at the yield point, signifying the end of elastic deformation (see Fig. 4(b)). As strain continues to accumulate, deformation twin begins to takes place and accommodate the plasticity together with dislocation. The twins thicken through the motion of  $1/3[\bar{1}\bar{1}\bar{1}](112)$  edge dislocation. This process, known as anti-twinning, contributes to the overall plastic behavior. The details are shown in the zoom-in picture of anti-twinning Fig. 4(c), and similar phenomenon has also been identified in nanoscale tungsten [5].

Under compressive loading, strain firstly induces the aggregation of vacancies to form the rod-shaped vacancy cluster defect on  $(\bar{1}\bar{1}2)$ . In Fig. 4(d), the formed  $(\bar{1}\bar{1}2)$  vacancy cluster defect suddenly collapses from its center, leading to the formation of a vacancy dislocation loop [54]. Then, the  $1/2[11\bar{1}]$  screw dislocation loop expand on the  $(\bar{1}\bar{1}2)$  plane as the stress increases. The gliding screw dislocation impinges upon one of the vacancies on  $(\bar{1}\bar{1}2)$  plane, which strongly arrests its motion. This triggers the dissociation of screw dislocation and the beginning of twin nucleation. The zoom-in pictures of subsequently

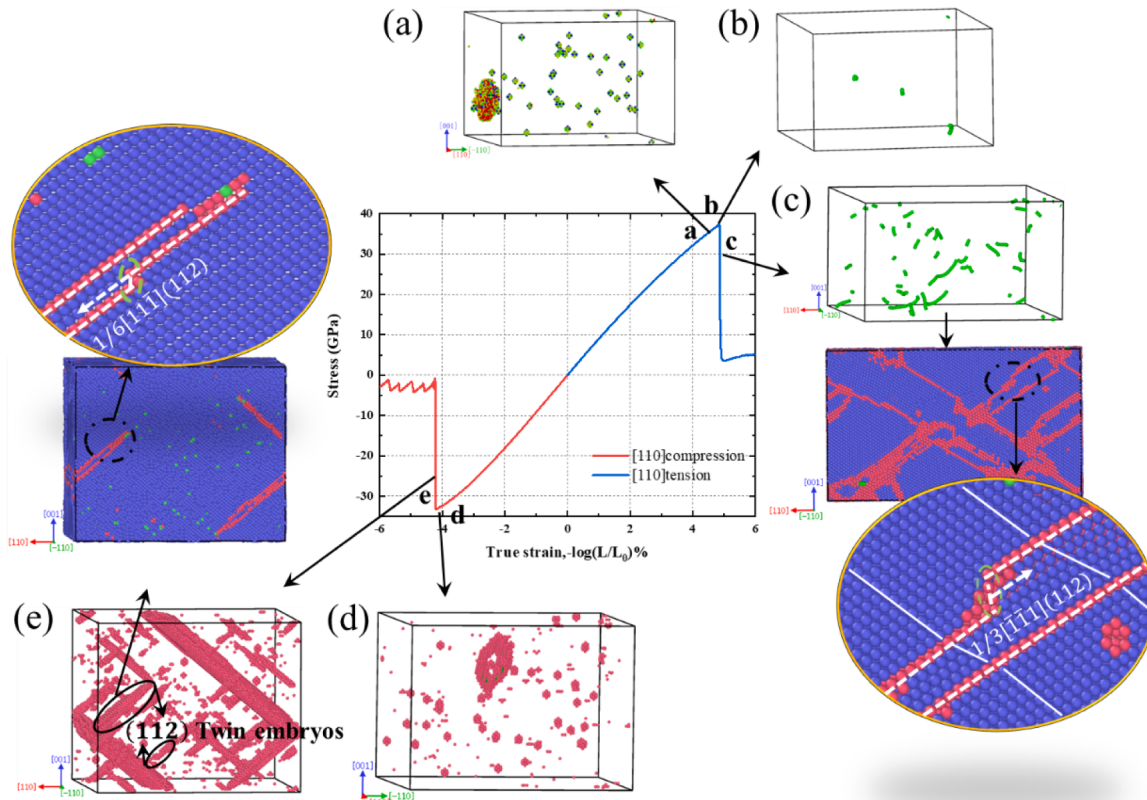


**Fig. 4.** Snapshots of atomistic configuration during tension deformation process ((a) $\epsilon = 4.47\%$ , (b) $\epsilon = 4.84\%$ , (c) $\epsilon = 4.87\%$ ) and compression deformation process ((d) $\epsilon = -4.04\%$ , (e) $\epsilon = -4.22\%$ ) at strain rate  $10^8 \text{ s}^{-1}$  along [110] orientation (vacancy concentration 0.02 %).

formed  $1/6[111](11\bar{2})$  twins are shown in Fig. 4(e). According to the twinning mode, the ordinary twins thicken through successive gliding of  $b = 1/6 [111]$  disconnections on adjacent  $(11\bar{2})$  planes which is half of that in anti-twinning mode under tensile condition [55,56].

### (3) Loading along [111]

When the stress is applied parallel to the Burgers vector of the perfect dislocation, such as  $1/2\langle 111 \rangle$  for BCC in our case, the emission of dislocation loops becomes the dominant deformation mechanism [40, 57]. In uniaxial tensile loading along [111], shown in Fig. 5(a), two leading partial dislocations with burgers vector  $\langle 1\bar{1}\bar{1} \rangle a/2$  are emitted on  $(110)$  plane. At yield point, in Fig. 5(b), numerous dislocation loops extend along the two  $\{110\}$  planes, causing a sharp drop of the stress. After yielding, the  $1/6[111]$  partial dislocation triggers the formation of  $1/6[111](11\bar{2})$  twins, as shown in the zoom-in picture of Fig. 5(c). This may be because the lower dislocation density can no longer accommodate plastic deformation, so twinning is activated. The similar behavior of dislocation loops emission is also observed in uniaxial compression loading, shown in Fig. 5(d)-(e), and there is no twin nucleation event happening here.

### (4) Loading along [112]

Despite the anisotropy of plasticity in tungsten has been investigated widely, plastic deformation mechanisms along [112] loading orientation have received limited attention in the literature. For tensile loading, the coalescence of vacancies occurs at the corners of the crystal, leading to the formation of large lamellar stacking faults on the  $(11\bar{2})$  plane as shown in Fig. 6(a) and (b). During yielding, several vacancy clusters form from the large lamellar stacking faults and then suddenly collapse

from its center position due to its instability, and eventually turns into oval-shaped dislocation loops on  $\{110\}$  planes. Plastic response of vacancies under loading along [112] mirrors the observed pattern in the [111] direction that the plastic deformation is dominated by the nucleation of dislocation in  $(110)$  plane as shown in Fig. 6(d)-(e). The red atoms in the box edges are linear segregation of vacancies, which will participate into plastic deformation with dislocation glide and twinning.

To gain deep insight into the evolution of defects during uniaxial tensile and compressive loading, we dig into the relationship between vacancy numbers and defects densities, as is shown in Fig. 7. The defect density was calculated based on the major defect type in that system. For example, dislocation density is used for [111] and [112] loadings, as slip dominates the plastic deformation in these two systems. While for loading along [100], the deformation twin and dislocation are adopted for tensile and compression conditions, respectively, since their density found in Fig. 3. The deformation twin and dislocation are adopted for compression and tensile conditions in [110].

The dashed lines depicted in Fig. 7 delineate the critical points marking the onset of yielding. For the left of these lines, the pink-colored blocks symbolize the strain distribution associated with vacancy evolution before yielding, whereas the green-colored blocks to the right represent the strain distribution during the yielding process. A comprehensive analysis of changes in vacancy numbers (indicated by black lines) and defect densities (illustrated by red lines) reveals several key observations. Firstly, during the elastic period, several vacancies interact with each other and result in the formation of vacancy cluster defects. Only few dislocations or twins can be observed in this stage. Secondly, upon reaching the yielding point, a marked decline in vacancy numbers occurs. Simultaneously, there is a rapid escalation in defect density, and then achieving saturation within a brief temporal span. This phenomenon signifies that the coalescence of vacancies, which is driven

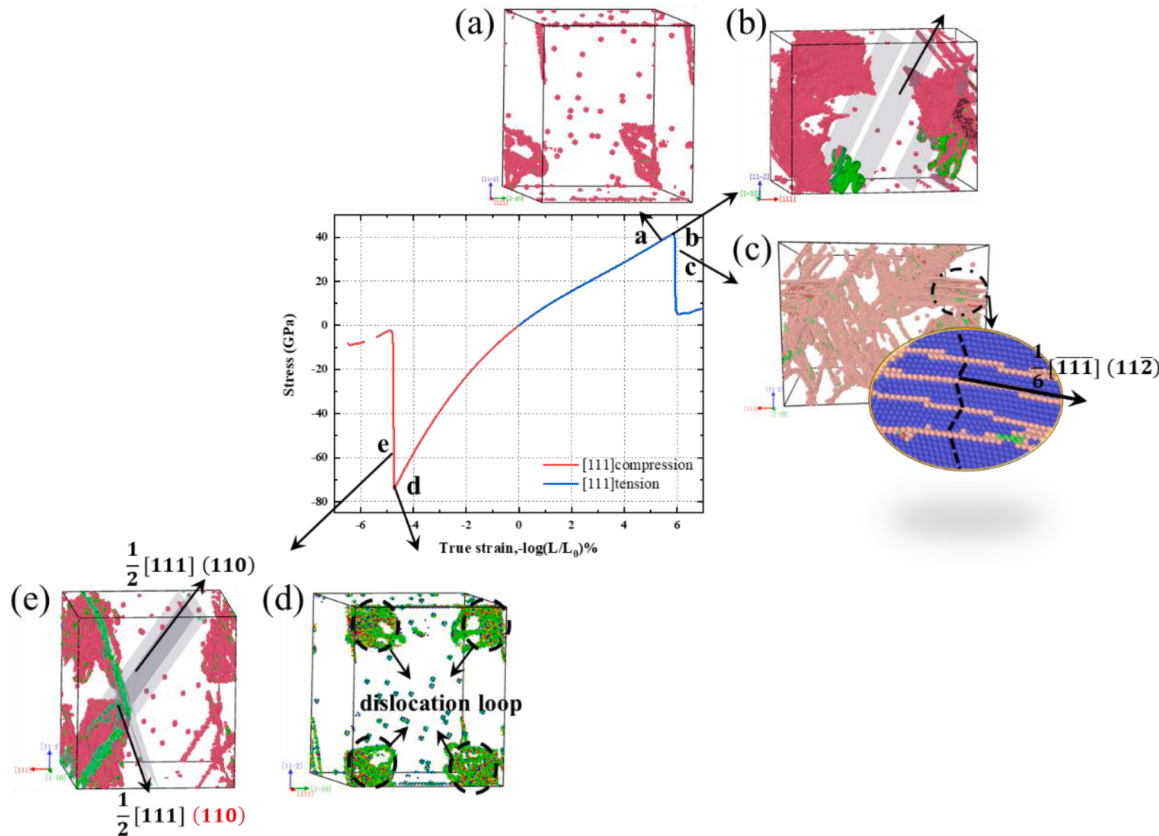


**Fig. 5.** Snapshots of atomistic configuration during tension deformation process ((a) $\epsilon = 5.42\%$ , (b) $\epsilon = 5.86\%$ , (c) $\epsilon = 5.91\%$ ) and compression deformation process ((d) $\epsilon = -4.73\%$ , (e) $\epsilon = -4.75\%$ ) at strain rate  $10^8 \text{ s}^{-1}$  along [111] orientation (vacancy concentration 0.02 %).

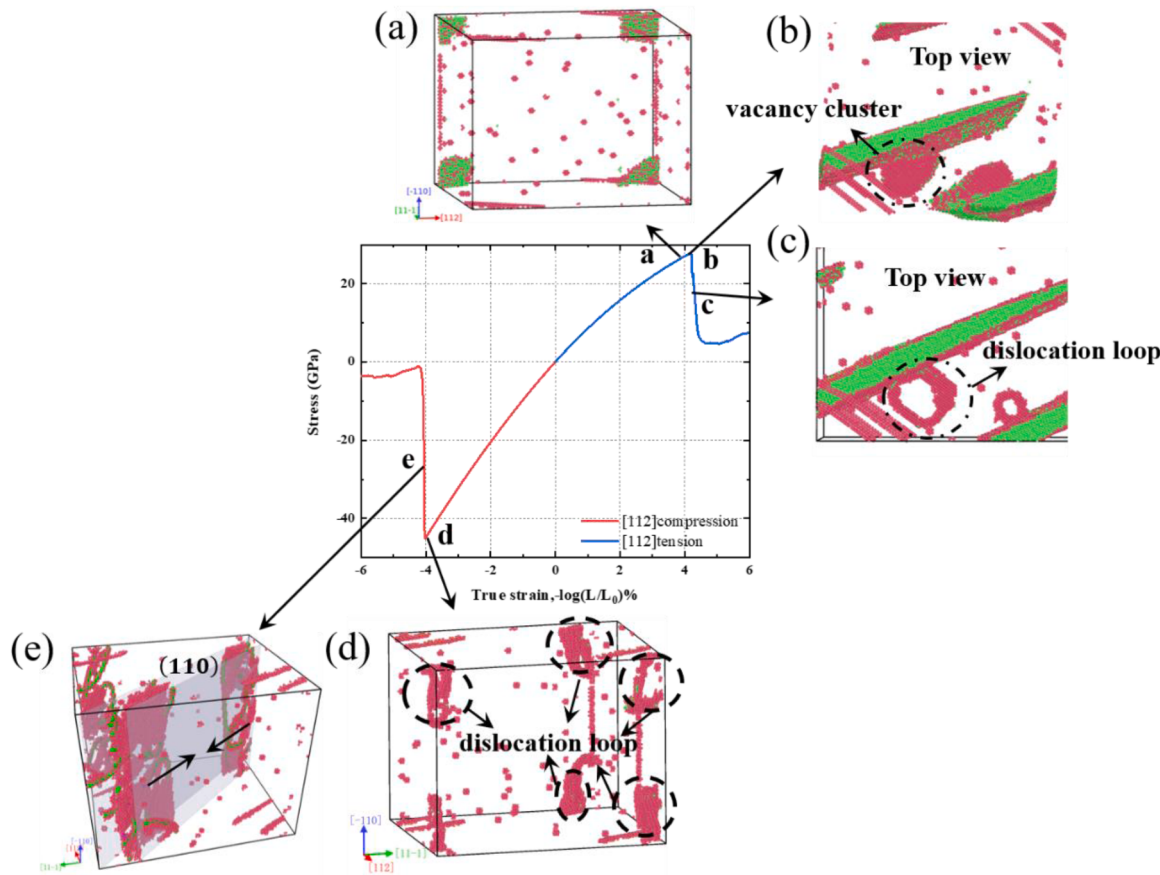


**Fig. 6.** Snapshots of atomistic configuration during tension deformation process ((a)  $\varepsilon = 3.85\%$ , (b)  $\varepsilon = 4.19\%$ , (c)  $\varepsilon = 4.29\%$ ) and compression deformation process ((d)  $\varepsilon = -4.02\%$ , (e)  $\varepsilon = -4.06\%$ ) at strain rate  $10^8 \text{ s}^{-1}$  along [112] orientation (vacancy concentration 0.02 %).

by external stress and serves as the origin for the evolution of defects.

On the other hand, these microstructure defect densities serve as indicators of the macroscopic stress, as illustrated in Fig. 2. For instance, in the left side of Fig. 7(a-d), loading along [111] orientation exhibits the highest dislocation density during the plastic deformation, while the [112] orientation has the lowest dislocation density. The dislocation density for [100] falls between these extremes. This observed trend aligns with the corresponding flow stress in Fig. 2, where  $\sigma_y([111]) > \sigma_y([100]) > \sigma_y([112])$ . We also found the dislocation density recorded in Fig. 7 agree well with that from experiment of bcc materials which ranges from  $10^{11}$  to  $10^{13} \text{ cm}^{-2}$  [58]. For example, Chen et al. [59] investigated the deformation mechanism of nanocrystalline Mo under high pressure torsion. The maximum dislocation density reached is  $2.5 \times 10^{12} \text{ cm}^{-2}$  at the grain size of  $\sim 75 \text{ nm}$  that is similar to dislocation density we observed in [110] and [112] orientations.

In addition, the plastic deformation for compression along [110] is twinning, resulting in a yield stress even smaller than that observed in [112]. The right side of Fig. 7(a-d) display the defect density under tensile loading. Similar to compressive loading, the [111] orientation still has the highest dislocation density, but there is a slight decrease in dislocation density at the later stages of yielding. This could be attributed to the nucleation of twins as shown in Fig. 5(c). Although the dislocation density of loading along [112] orientation is larger than that in [110], the [110] shows a higher yield stress than [112]. This unconventional observation may be attributed to the nucleation of anti-twinning, where overcoming the energy barrier for anti-twinning shear requires more energy than twinning shear or dislocation slip.

#### 4. Discussion

The vacancies evolution in tension-compression asymmetry, like those published in the previous literature [5,9,32,60] and discussed in Section 3.2, introduces colorful plastic mechanisms along different crystallographic orientations. A fundamental question is whether the resolved stress required for dislocation motion before plastic deformation is consistent with the tension-compression asymmetry observed in Fig. 2. In history, many researchers have studied the glide of screw dislocation through MD simulations by using tight-binding based Bond Order potentials and some other central force potentials [45,61,62]. To investigate the tension-compression asymmetry, the effect of tensile and compressive loading on the  $1/2[111]$  screw dislocation was carried out for four different axes of tension and compression for tungsten with vacancies, which are shown in the [001] stereographic projection in Fig. 8. They were chosen within the standard triangle such that the corresponding MRSSPs concur with the following planes:  $(\bar{1}01)$  for the loading axes  $[238]$  and  $[012]$ ,  $(\bar{1}\bar{1}2)$  for the loading axis  $[001]$  and  $(\bar{2}11)$  for the loading axis  $[011]$ , respectively. For the loading axis  $[011]$ , the shear in the  $(\bar{2}11)$  plane is in the twinning sense for compression and anti-twinning sense for tension [44]. Here, the loading axes  $[238]$  and  $[012]$  are chosen to represent the [111] and [112] loading orientation in this study. Because the dislocation mainly slips on  $\{110\}$  for loading along [111] and [112], which is consistent with the MRSSPs for loading axes  $[238]$  and  $[012]$ . Intuitively, the loading axes  $[001]$  and  $[011]$  are chosen to represent the planes where deformation happens for loading along [100] and [110] in Figs. 3 and 4, respectively.

Fig. 9 presents the calculated critical resolved shear stress (CRSS) on the maximum resolved shear stress plane (MRSSP) for the  $1/2[111]$  screw dislocation under tension (blue pillars) and compression (green

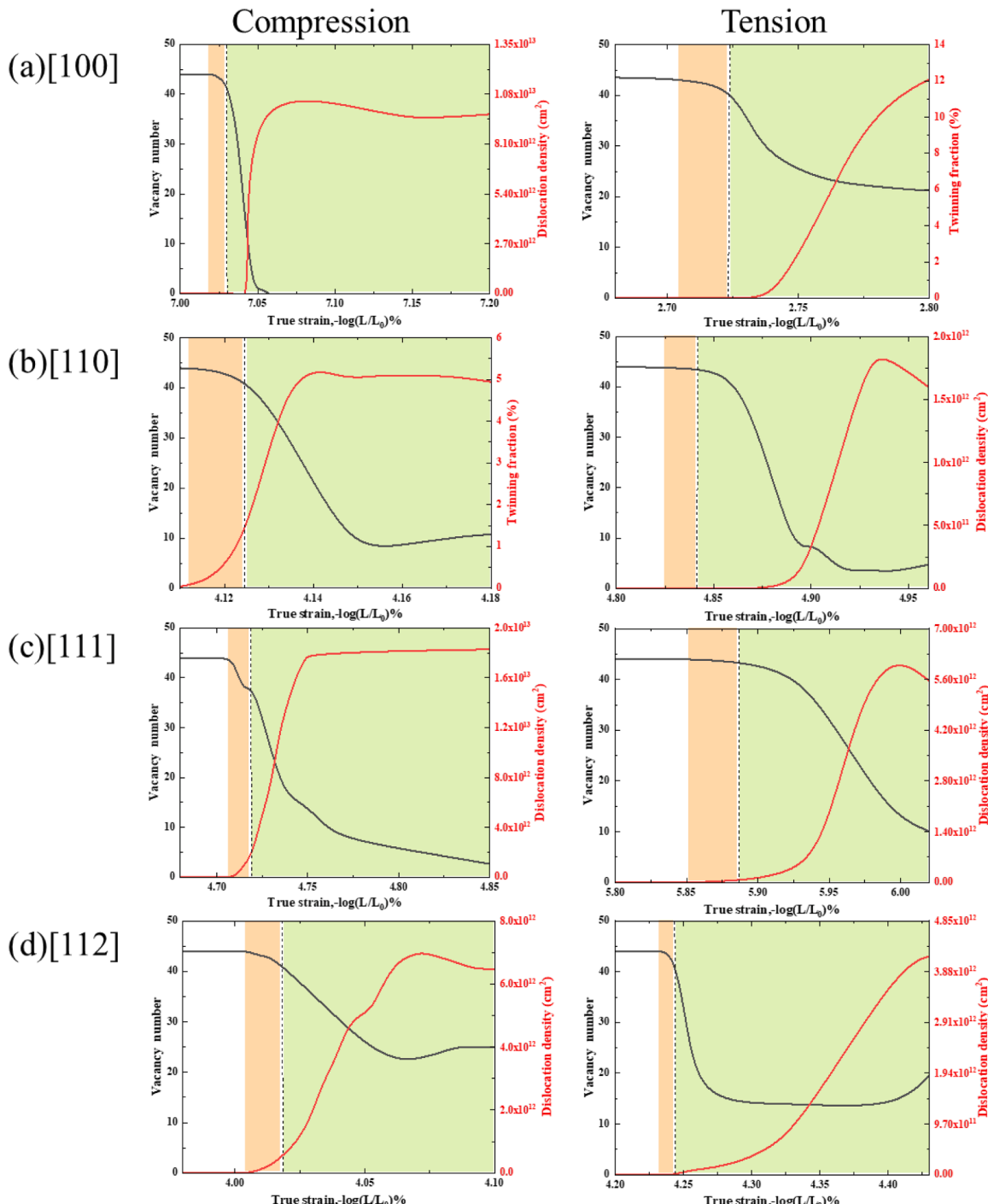


**Fig. 7.** Relationship between the number of vacancy and defect density as a function of true strain under tensile and compressive loading along different orientations at strain rate  $10^8 \text{ s}^{-1}$ , respectively (vacancy concentration 0.02 %).

pillars) across various orientations and strain rates. A pronounced tension-compression asymmetry in CRSS was observed, with compressive CRSS values consistently surpassing those under tensile loading, irrespective of orientation. Notably, the unusual tension-compression asymmetry observed in the [110] orientation was confirmed. For loading along the [011] axis, the CRSS reaches 1.23 GPa under shear on the  $\{\bar{2}11\}$  plane in the twinning mode during compression, compared to 2.31 GPa in the anti-twinning mode under tension. This inverted asymmetry along the [011] axis can be attributed to differences in energy landscapes between anti-twinning and ordinary twinning mechanisms [5,10] and the associated unstable stacking fault energy [63]. For

the remaining loading axes, plastic deformation is primarily driven by dislocation slip on  $\{110\}$  planes, where shear stress perpendicular to the slip direction significantly influences tension-compression asymmetry. Specifically, the negative perpendicular shear stress under compression elevates lattice friction, whereas the positive perpendicular shear stress under tension reduces lattice friction, resulting in higher CRSS values during compressive loading. Notably, the CRSS values derived from our simulations are consistent with experimentally measured yield strengths for materials under irradiation conditions. For instance, experimental data on tungsten [64] under irradiation report yield strengths around 1.5 GPa at 300 K.

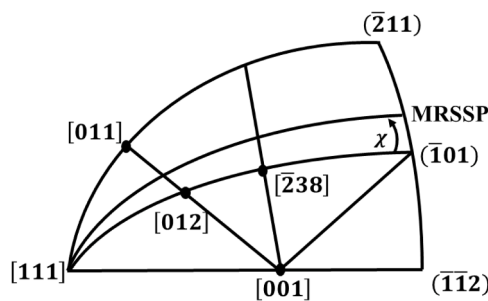


**Fig. 8.** [001] stereographic projection showing the orientation of the four tension and compression axes used in the study of the effect of uniaxial loading.

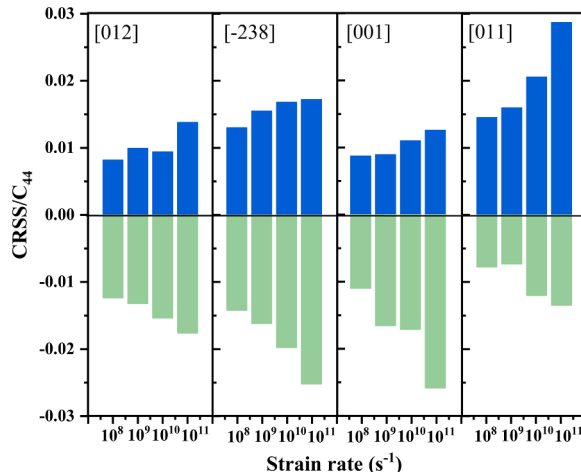


**Fig. 9.** CRSS on the MRSSP for the  $\frac{1}{2}[111]$  screw dislocation in W loaded in tension or compression for different orientations of the tensile or compressive axis at different strain rates (vacancy concentration 0.02 %).

Secondly, the strain rates ( $10^8$ ,  $10^9$ ,  $10^{10}$  and  $10^{11} \text{ s}^{-1}$ ) also play a role in motion screw dislocation core. In Fig. 9, the CRSSs on the MRSSP for the  $1/2[111]$  screw dislocation exhibits a strong dependence on strain rates. The CRSS for the dislocation core increases with higher strain rates. This increment of CRSS with respect to strain rate follows a nonlinear relationship, showing an Arrhenius thermal activation process and affected by phonon drag [49]. This means the yield strength follows a power law as a function of strain rate.

For loading axes [-238] (or [111]) and [012] (or [112]) where dislocation slip dominates the deformation, the higher CRSS on the MRSSP indicates increased resistance to dislocation movement on the corresponding  $\{110\}$  planes. The CRSSs for loading axis [-238] which represent the [111] loading orientation in Section 3.1 and 3.2 exceed those for the [012] axis under both compressive and tensile loading, highlighting the greater difficulty in dislocation activity in this orientation. For tensile loading along axis [011], the CRSSs are greatly larger than those in compressive loading, indicating that the anti-twinning shear mediated by the glide of  $1/3\langle111\rangle\{112\}$  dislocation presents a considerably greater challenge compared to ordinary twinning. Consequently, a specific tension-compression asymmetry is shown in Fig. 2 that the yield stress for tensile along [110] orientation is larger than that for compressive loading.

## 5. Conclusions

The heterogeneous nucleation and tension-compression asymmetry behaviors of pre-existing vacancies embedded in monocrystal tungsten subjected to loading along different crystallographic orientation, vacancy concentration and strain rates were studied through molecular

dynamics simulation. The major findings are as follows.

- (1) The tension-compression asymmetry is strongly related to the crystallographic orientation. Based on the gap of yield stress of compressive and tensile loading, the tension-compression asymmetry intensity is in a sequence of  $[111] > [112] > [110] > [100]$ . Even though pre-existing vacancies do not alter the tension-compression asymmetry along different loading directions, they reduce the extent of tension-compression asymmetry by narrowing the gap of yield stress of compressive and tensile loading.
- (2) The tension-compression asymmetry is due to the distinct plastic deformation behaviors for compressive and tensile loading. The existence of vacancy facilitates the nucleation and evolution of crystal defects during plastic deformation. Aggregation, coalescence and growth of vacancies before yielding determines the plastic behaviors along various loading directions. That is the faster the vacancy condensation, the higher the defect concentration. As a result, the larger the gap of the defect densities, the wider the tension-compression asymmetry. The defect details are for the case of [111] and [112] slips dominate the deformation. As for [100] and [110], both twinning or dislocation slip lead to yielding for compressive and tensile loading. Nevertheless, the occurrence of anti-twinning in [110] under tensile loading results a higher yielding stress over compression.
- (3) Owing to the non-planar cores,  $1/2\langle111\rangle$  screw dislocation is identified as the manipulator behind those plastic deformations. The CRSSs on the MRSSP for the  $1/2[111]$  screw dislocation loaded in tension and compression are found responsible for the tension-compression asymmetry in those loading axis studied. The CRSS in tension will be always lower than that in compression for [-238], [012] and [001] loading axis, resulting in the larger compression stress over tensile stress along [111], [112] and [100], respectively. For loading along [110], the CRSS in tension is higher than that in compression, accounting for the abnormal tension over compression behavior.

These findings shed lights on the atomic-scale mechanisms underlying the tension-compression asymmetry behavior in tungsten with pre-existing vacancies and provide valuable insights into the deformation behavior of crystalline materials under different loading conditions.

## CRediT authorship contribution statement

**Ziyi Li:** Writing – original draft, Visualization, Validation, Investigation, Formal analysis, Data curation, Conceptualization. **Wensheng Liu:** Writing – review & editing, Visualization, Project administration, Methodology, Conceptualization. **Yunzhu Ma:** Writing – review & editing, Project administration, Funding acquisition, Formal analysis, Conceptualization. **Chaoping Liang:** Writing – review & editing, Visualization, Validation, Supervision, Software, Project administration, Methodology, Investigation, Funding acquisition, Formal analysis, Conceptualization.

## Declaration of competing interest

The authors declare that they have no known competing financial interests or personal relationships that could have appeared to influence the work reported in this paper.

## Acknowledgments

This work was supported by the National Natural Science Foundation of China (grant numbers 51801236, 51931012, 52471026) and Natural Science Foundation of Hunan Province (grant number 2025JJ20048).

We are grateful for technical support from the High Performance Computing Center of Central South University.

## Supplementary materials

Supplementary material associated with this article can be found, in the online version, at [doi:10.1016/j.jnucmat.2025.155806](https://doi.org/10.1016/j.jnucmat.2025.155806).

## Data availability

Data will be made available on request.

## References

- [1] M. Rieth, S.L. Dudarev, Recent progress in research on tungsten materials for nuclear fusion applications in Europe, *J. Nucl. Mater.* 432 (2013) 482–500, <https://doi.org/10.1016/j.jnucmat.2012.08.018>.
- [2] E. Lassner, W.-D. Schubert, *Tungsten: properties, chemistry, Technology of the elements, alloys, and Chemical Compounds*, Springer Science & Business Media, 1999.
- [3] R. Gröger, V. Racherla, J.L. Bassani, V. Vitek, Multiscale modeling of plastic deformation of molybdenum and tungsten: II. Yield criterion for single crystals based on atomistic studies of glide of 1/2 ⟨111⟩ screw dislocations, *Acta Mater.* 56 (2008) 5412–5425, <https://doi.org/10.1016/j.actamat.2008.07.037>.
- [4] J.Y. Kim, D. Jang, J.R. Greer, Tensile and compressive behavior of tungsten, molybdenum, tantalum and niobium at the nanoscale, *Acta Mater.* 58 (2010) 2355–2363, <https://doi.org/10.1016/j.actamat.2009.12.022>.
- [5] J. Wang, Z. Zeng, M. Wen, Q. Wang, D. Chen, Y. Zhang, P. Wang, H. Wang, Z. Zhang, S.X. Mao, T. Zhu, Anti-twining in nanoscale tungsten, *Sci. Adv.* 6 (2020), <https://doi.org/10.1126/sciadv.aay2792>.
- [6] F.E. Neumann, O.E. Meyer, *Vorlesungen über die theorie der Elasticität der festen Körper und des Lichtäthers*, BG Teubner, 1885.
- [7] J.Y. Kim, J.R. Greer, Tensile and compressive behavior of gold and molybdenum single crystals at the nano-scale, *Acta Mater.* 57 (2009) 5245–5253, <https://doi.org/10.1016/j.actamat.2009.07.027>.
- [8] G.J. Irwin, F. Guij, P.L. Pratt, The influence of orientation on slip and strain hardening of molybdenum single crystals, *Phys. Status Solidi. 22* (1974) 685–698, <https://doi.org/10.1002/pssa.2210220236>.
- [9] C.J. Healy, G.J. Ackland, Molecular dynamics simulations of compression-tension asymmetry in plasticity of Fe nanopillars, *Acta Mater.* 70 (2014) 105–112, <https://doi.org/10.1016/j.actamat.2014.02.021>.
- [10] G. Wei, H. Xie, F. Yin, G. Lu, Twinning mechanism asymmetry in body-centered cubic tantalum under [001]uniaxial compression/tension, *Phys. Rev. Mater.* 5 (2021) 123604, <https://doi.org/10.1103/PhysRevMaterials.5.123604>.
- [11] Z.Q. Wang, I.J. Beyerlein, An atomistically-informed dislocation dynamics model for the plastic anisotropy and tension-compression asymmetry of BCC metals, *Int. J. Plast.* 27 (2011) 1471–1484, <https://doi.org/10.1016/j.ijplas.2010.08.011>.
- [12] N. Bertin, L.A. Zepeda-Ruiz, V.V. Bulatov, Sweep-tracing algorithm: in silico slip crystallography and tension-compression asymmetry in BCC metals, *Mater. Theory.* 6 (2022) 1–23, <https://doi.org/10.1186/s41313-021-00031-7>.
- [13] S.L. Dudarev, J.L. Bourtad, R. Lässer, M.J. Caturla, P.M. Derlet, M. Fivel, C.C. Fu, M.Y. Lavrentiev, L. Malerba, M. Mrovec, D. Nguyen-Manh, K. Nordlund, M. Perlado, R. Schäublin, H. Van Swygenhoven, D. Terentyev, J. Wallenius, D. Weygand, F. Willaime, The EU programme for modelling radiation effects in fusion reactor materials: an overview of recent advances and future goals, *J. Nucl. Mater.* 386–388 (2009) 1–7, <https://doi.org/10.1016/j.jnucmat.2008.12.301>.
- [14] J.C. Haley, F. Liu, E. Tarleton, A.C.F. Cocks, G.R. Odette, S. Lozano-Perez, S. G. Roberts, Helical dislocations: observation of vacancy defect bias of screw dislocations in neutron irradiated Fe–9Cr, *Acta Mater.* 181 (2019) 173–184, <https://doi.org/10.1016/j.actamat.2019.09.031>.
- [15] X.Z. Tang, Y.F. Guo, Y. Fan, S. Yip, B. Yıldız, Interstitial emission at grain boundary in nanolayered alpha-Fe, *Acta Mater.* 105 (2016) 147–154, <https://doi.org/10.1016/j.actamat.2015.12.009>.
- [16] M. Samaras, Atomic scale modelling of the primary damage state of irradiated fcc and bcc nanocrystalline metals, 351 (2006) 47–55. <https://doi.org/10.1016/j.jnucmat.2006.02.030>.
- [17] W.G. Wolfer, M. Ashkin, Diffusion of vacancies and interstitials to edge dislocations, *J. Appl. Phys.* 47 (1976) 791–800, <https://doi.org/10.1063/1.322710>.
- [18] M.C. Marinica, L. Ventelon, M.R. Gilbert, L. Proville, S.L. Dudarev, J. Marian, G. Beneteux, F. Willaime, Interatomic potentials for modelling radiation defects and dislocations in tungsten, *J. Phys. Condens. Matter.* 25 (2013), <https://doi.org/10.1088/0953-8984/25/39/395502>.
- [19] S.J. Zinkle, Y. Matsukawa, Observation and analysis of defect cluster production and interactions with dislocations, *J. Nucl. Mater.* 329–333 (2004) 88–96, <https://doi.org/10.1016/j.jnucmat.2004.04.298>.
- [20] Y. Li, L. Wang, G. Ran, Y. Yuan, L. Wu, X. Liu, X. Qiu, Z. Sun, Y. Ding, Q. Han, X. Wu, H. Deng, X. Huang, In-situ TEM investigation of 30 keV he+ irradiated tungsten: effects of temperature, fluence, and sample thickness on dislocation loop evolution, *Acta Mater.* 206 (2021), <https://doi.org/10.1016/j.actamat.2020.116618>.
- [21] S. Fukuzumi, T. Yoshiie, Y. Satoh, Q. Xu, H. Mori, M. Kawai, Defect structural evolution in high purity tungsten irradiated with electrons using high voltage electron microscope, *J. Nucl. Mater.* 343 (2005) 308–312, <https://doi.org/10.1016/j.jnucmat.2004.11.019>.
- [22] H. Iwakiri, K. Yasunaga, K. Morishita, N. Yoshida, Microstructure evolution in tungsten during low-energy helium ion irradiation, *J. Nucl. Mater.* 283–287 (2000) 1134–1138, [https://doi.org/10.1016/S0022-3115\(00\)00289-0](https://doi.org/10.1016/S0022-3115(00)00289-0).
- [23] G. Valles, M. Panizo-Laiz, C. González, I. Martín-Bragado, R. González-Arrabal, N. Gordillo, R. Iglesias, C.L. Guerrero, J.M. Perlado, A. Rivera, Influence of grain boundaries on the radiation-induced defects and hydrogen in nanostructured and coarse-grained tungsten, *Acta Mater.* 122 (2017) 277–286, <https://doi.org/10.1016/j.actamat.2016.10.007>.
- [24] C.G. Zhang, W.H. Zhou, Y.G. Li, Z. Zeng, X. Ju, Primary radiation damage near grain boundary in bcc tungsten by molecular dynamics simulations, *J. Nucl. Mater.* 458 (2015) 138–145, <https://doi.org/10.1016/j.jnucmat.2014.11.135>.
- [25] J. Fu, Y. Chen, J. Fang, N. Gao, W. Hu, C. Jiang, H.B. Zhou, G.H. Lu, F. Gao, H. Deng, Molecular dynamics simulations of high-energy radiation damage in W and W-Re alloys, *J. Nucl. Mater.* 524 (2019) 9–20, <https://doi.org/10.1016/j.jnucmat.2019.06.027>.
- [26] A.E. Sand, S.L. Dudarev, K. Nordlund, High-energy collision cascades in tungsten: dislocation loops structure and clustering scaling laws, *EPL* 103 (2013), <https://doi.org/10.1209/0295-5075/103/46003>.
- [27] Z.Z. Li, Y.H. Li, D. Terentyev, N. Castin, A. Bakaev, G. Bonny, Z. Yang, L. Liang, H. B. Zhou, F. Gao, G.H. Lu, Investigating the formation mechanism of void lattice in tungsten under neutron irradiation: from collision cascades to ordered nanovoids, *Acta Mater.* 219 (2021) 117239, <https://doi.org/10.1016/j.actamat.2021.117239>.
- [28] X. Li, W. Liu, Y. Xu, C.S. Liu, Q.F. Fang, B.C. Pan, J.L. Chen, G.N. Luo, Z. Wang, An energetic and kinetic perspective of the grain-boundary role in healing radiation damage in tungsten, *Nucl. Fus.* 53 (2013), <https://doi.org/10.1088/0029-5515/53/12/123014>.
- [29] C. Reina, J. Marian, M. Ortiz, Nanovoid nucleation by vacancy aggregation and vacancy-cluster coarsening in high-purity metallic single crystals, *Phys. Rev. B - Condens. Matter Mater. Phys.* 84 (2011) 1–12, <https://doi.org/10.1103/PhysRevB.84.104117>.
- [30] S. Li, Y. Li, Y.C. Lo, T. Neeraj, R. Srinivasan, X. Ding, J. Sun, L. Qi, P. Gumbusch, J. Li, The interaction of dislocations and hydrogen-vacancy complexes and its importance for deformation-induced proto nano-voids formation in α-Fe, *Int. J. Plast.* 74 (2015) 175–191, <https://doi.org/10.1016/j.ijplas.2015.05.017>.
- [31] W.W. Pang, P. Zhang, G.C. Zhang, A.G. Xu, X.G. Zhao, Dislocation creation and void nucleation in FCC ductile metals under tensile loading: a general microscopic picture, *Sci. Rep.* 4 (2014) 1–7, <https://doi.org/10.1038/srep06981>.
- [32] A. Dutta, Compressive deformation of Fe nanopillar at high strain rate: modalities of dislocation dynamics, *Acta Mater.* 125 (2017) 219–230, <https://doi.org/10.1016/j.actamat.2016.11.062>.
- [33] S. Plimpton, Fast parallel algorithms for short-range molecular dynamics for the United States Department of Energy under contract DE-AC04-76DOO789, *J. Comput. Phys.* 117 (1995) 1–19.
- [34] X.W. Zhou, R.A. Johnson, H.N.G. Wadley, Misfit-energy-increasing dislocations in vapor-deposited CoFe/NiFe multilayers, *Phys. Rev. B* 69 (2004) 144113, <https://doi.org/10.1103/PhysRevB.69.144113>.
- [35] W. Wei, L. Chen, H.R. Gong, J.L. Fan, Strain-stress relationship and dislocation evolution of W-Cu bilayers from a constructed n-body W-Cu potential, *J. Phys. Condens. Matter.* 31 (2019), <https://doi.org/10.1088/1361-648X/ab1a8a>.
- [36] G.C. Ma, J.L. Fan, H.R. Gong, Mechanical behavior of Cu-W interface systems upon tensile loading from molecular dynamics simulations, *Comput. Mater. Sci.* 152 (2018) 165–168, <https://doi.org/10.1016/j.commatsci.2018.05.030>.
- [37] Y.J. Shen, L.C. Liu, S.T. Mi, H.R. Gong, S.F. Zhou, Construction of an n-body Fe-Cu potential and its application in atomistic modeling of Fe-Cu solid solutions, *J. Appl. Phys.* 127 (2020), <https://doi.org/10.1063/1.5129015>.
- [38] S.T. Mi, H.R. Gong, J.L. Fan, Structural stability and mechanical property of Fe-W solid solutions from a constructed Fe-W potential, *J. Appl. Phys.* 126 (2019), <https://doi.org/10.1063/1.5111093>.
- [39] L. Chen, J.L. Fan, H.R. Gong, Phase transition and mechanical properties of tungsten nanomaterials from molecular dynamic simulation, *J. Nanoparticle Res.* 19 (2017), <https://doi.org/10.1007/s11051-017-3812-z>.
- [40] W. Liu, Z. Li, X. Bai, Y. Ma, C. Liang, A unified model for yield strength and plastic behavior of nanovoid evolution in tungsten based on molecular dynamics simulations, *Comput. Mater. Sci.* 211 (2022) 111534, <https://doi.org/10.1016/j.commatsci.2022.111534>.
- [41] A. Stukowski, Visualization and analysis of atomistic simulation data with OVITO-the Open Visualization Tool, *Model. Simul. Mater. Sci. Eng.* 18 (2010), <https://doi.org/10.1088/0965-0393/18/1/015012>.
- [42] J.D. Honeycutt, H.C. Andersen, Molecular dynamics study of melting and freezing of small Lennard-Jones clusters, *J. Phys. Chem.* 91 (1987) 4950–4963, <https://doi.org/10.1021/j100303a014>.
- [43] A. Stukowski, K. Albe, Extracting dislocations and non-dislocation crystal defects from atomistic simulation data, *Model. Simul. Mater. Sci. Eng.* 18 (2010) 085001, <https://doi.org/10.1088/0965-0393/18/8/085001>.
- [44] K. Ito, V. Vitek, Atomistic study of non-Schmid effects in the plastic yielding of bcc metals, *Philos. Mag. A Phys. Condens. Matter, Struct. Defects Mech. Prop.* 81 (2001) 1387–1407, <https://doi.org/10.1080/01418610108214447>.
- [45] R. Gröger, A.G. Bailey, V. Vitek, Multiscale modeling of plastic deformation of molybdenum and tungsten: I. Atomistic studies of the core structure and glide of 1/2⟨111⟩ screw dislocations at 0 K, *Acta Mater.* 56 (2008) 5401–5411, <https://doi.org/10.1016/j.actamat.2008.07.018>.

- [46] J.P. Hirth, J. Lothe, T. Mura, Theory of dislocations, *J. Appl. Mech.* 50 (1983) 476–477.
- [47] L.M. Hale, C.A. Becker, Vacancy dissociation in body-centered cubic screw dislocation cores, *Comput. Mater. Sci.* 135 (2017) 1–8, <https://doi.org/10.1016/j.commatsci.2017.02.033>.
- [48] N. Zotov, B. Grabowski, Molecular dynamics simulations of screw dislocation mobility in bcc Nb, *Model. Simul. Mater. Sci. Eng.* 29 (2021), <https://doi.org/10.1088/1361-651X/ac2b02>.
- [49] Y. Tang, Uncovering the inertia of dislocation motion and negative mechanical response in crystals, *Sci. Rep.* 8 (2018) 1–15, <https://doi.org/10.1038/s41598-017-18254-5>.
- [50] J.Y. Kim, D. Jang, J.R. Greer, Crystallographic orientation and size dependence of tension-compression asymmetry in molybdenum nano-pillars, *Int. J. Plast.* 28 (2012) 46–52, <https://doi.org/10.1016/j.ijplas.2011.05.015>.
- [51] L.A. Zepeda-Ruiz, A. Stukowski, T. Oppelstrup, V.V. Bulatov, Probing the limits of metal plasticity with molecular dynamics simulations, *Nature* 550 (2017) 492–495, <https://doi.org/10.1038/nature23472>.
- [52] J. Monk, D. Farkas, Tension-compression asymmetry and size effects in nanocrystalline Ni nanowires, *Philos. Mag.* 87 (2007) 2233–2244, <https://doi.org/10.1080/14786430701361404>.
- [53] D. Farkas, A. Caro, E. Bringa, D. Crowson, Mechanical response of nanoporous gold, *Acta Mater.* 61 (2013) 3249–3256, <https://doi.org/10.1016/j.actamat.2013.02.013>.
- [54] S. Jiang, Y. Huang, K. Wang, X. Li, H. Deng, S. Xiao, W. Zhu, W. Hu, Effects of vacancies on plasticity and phase transformation in single-crystal iron under shock loading, *J. Appl. Phys.* 130 (2021), <https://doi.org/10.1063/5.0043880>.
- [55] N. Kvashin, P.L. García-Müller, N. Anento, A. Serra, Atomic processes of shear-coupled migration in {112} twins and vicinal grain boundaries in bcc-Fe, *Phys. Rev. Mater.* 4 (2020) 1–8, <https://doi.org/10.1103/PhysRevMaterials.4.073604>.
- [56] G. Wei, H. Xie, F. Yin, G. Lu, Twinning mechanism asymmetry in body-centered cubic tantalum under [001]uniaxial compression/tension, *Phys. Rev. Mater.* 5 (2021) 1–9, <https://doi.org/10.1103/physrevmaterials.5.123604>.
- [57] Y. Tang, E.M. Bringa, B.A. Remington, M.A. Meyers, Growth and collapse of nanovoids in tantalum monocrystals, *Acta Mater.* 59 (2011) 1354–1372, <https://doi.org/10.1016/j.actamat.2010.11.001>.
- [58] P. Thirathipviwat, G. Song, J. Bednarcik, U. Kühn, T. Gemming, K. Nielsch, J. Han, Compositional complexity dependence of dislocation density and mechanical properties in high entropy alloy systems, *Prog. Nat. Sci. Mater. Int.* 30 (2020) 545–551, <https://doi.org/10.1016/j.pnsc.2020.07.002>.
- [59] G.M. Cheng, W.W. Jian, W.Z. Xu, H. Yuan, P.C. Millett, Y.T. Zhu, Grain size effect on deformation mechanisms of nanocrystalline bcc metals, *Mater. Res. Lett.* 1 (2013) 26–31, <https://doi.org/10.1080/21663831.2012.739580>.
- [60] F. Zhang, J. Zhou, Tension-compression asymmetry and twin boundaries spacings effects in polycrystalline Ni nanowires, *J. Appl. Phys.* 120 (2016) 1–7, <https://doi.org/10.1063/1.4959206>.
- [61] R. Gröger, V. Vitek, Stress dependence of the Peierls barrier of  $1/2\langle 110 \rangle \langle 111 \rangle$  screw dislocations in bcc metals, *Acta Mater.* 61 (2013) 6362–6371, <https://doi.org/10.1016/j.actamat.2013.06.047>.
- [62] R. Gröger, V. Vitek, Impact of non-Schmid stress components present in the yield criterion for bcc metals on the activity of  $\{110\}\langle 111 \rangle$  slip systems, *Comput. Mater. Sci.* 159 (2019) 297–305, <https://doi.org/10.1016/j.jcommatsci.2018.12.021>.
- [63] D. Zhang, X. Liu, T. Li, K. Fu, Z. Peng, Y. Zhu, New insights of the strength asymmetry in FCC single-crystalline nanopillars, *Comput. Mater. Sci.* 208 (2022) 111360, <https://doi.org/10.1016/j.jcommatsci.2022.111360>.
- [64] S.A. Maloy, M.R. James, W. Sommer, G.J. Willcutt, M. Lopez, T.J. Romero, M. B. Toloczko, The effect of 800 MeV proton irradiation on the mechanical properties of tungsten at room temperature and at 475 °C, *J. Nucl. Mater.* 343 (2005) 219–226, <https://doi.org/10.1016/j.jnucmat.2004.12.018>.